Anion-Engineering Toward High-Voltage-Stable Halide Superionic Conductors for All-Solid-State Lithium Batteries

Liang Shen, Jin-Liang Li, Wei-Jin Kong, Chen-Xi Bi, Pan Xu, Xue-Yan Huang, Wen-Ze Huang, Fang Fu, Yi-Cheng Le, Chen-Zi Zhao, Hong Yuan, Jia-Qi Huang, and Qiang Zhang**

Halide solid electrolytes (SEs) are attracting strong attention as one of the compelling candidates for the next-generation of inorganic SEs due to their high ionic conductivity. Nevertheless, unsatisfactory high-voltage stability restricts the further applications of halide SEs. Herein, the anion-engineering of F^-/O^{2-} is evolved to construct the high-voltage stable zirconium-based halide superionic conductors ($Li_{2.5}ZrCl_5F_{0.5}O_{0.5}$, LZCFO). Benefiting from the thermodynamic/kinetic high-voltage stability of F-containing SE and the disordered localized structure introduced by O^{2-}, LZCFO displays a practical electrochemical limit of 4.87 V versus Li/Li^+ and an ionic conductivity of 1.17 mS cm^{-1} at 30 °C. With LZCFO and NCM955, the all-solid-state lithium battery exhibits a high discharge capacity of 207.1 mAh g^{-1} at 0.1C and a capacity retention of 81.2% after 500 cycles at 0.5C. The interfacial characterization further demonstrates the formation of the F-rich cathode–electrolyte interphase (CEI), which inhibits side reactions between the cathode and the SE and boosts excellent cycling stability. This work affords fresh insights on the engineering of SEs with high-voltage stability, high ionic conductivity, and stable CEI in all-solid-state lithium batteries.

1. Introduction

The explosive expansion of electronic devices and electric vehicles (EVs) propels the development of safe and high-energy-density batteries.[1] Compared to routine lithium-ion batteries (LIBs), all-solid-state lithium batteries (ASSLBs) are recognized as one of the most promising next-generation energy storage devices, because ALLSBs employ non-flammable inorganic solid electrolytes (SEs) instead of flammable organic electrolytes, which delivers greater safety and offers the potential for higher energy density by utilizing lithium metal anodes and high-voltage cathodes.[2]

SEs are one of the critical materials for ASSLBs and contribute decisively to the battery performance.[3] There have been many efforts to explore high-performance inorganic SEs and a variety of SEs candidates have been developed by solid ionic communities.[4] Sulfide SEs, such as $Li_7P_3S_{11}$,[5] $Li_{10}GeP_2S_{12}$,[6] and Li argyrodites $Li_{6-a}PS_{5-a}X_{1+a}$ (X = Cl, Br, I; $0 \leq a \leq 0.5$),[7] have attracted strong attention due to their ionic conductivity above 10^{-2} S cm^{-1} and excellent processing deformability.[8] However, because of the relatively low oxidation potential of sulfide SEs (usually around 2.5 V versus Li/Li^+), they are highly susceptible to decomposition and severe interfacial side reactions with high-voltage cathode active materials (CAMs) such as Ni-rich $LiMO_2$ (M = Ni, Co, Mn, and Al) during cycling, which significantly limits the capacity and cycling stability of ALLSBs.[9] Another type of inorganic SEs is oxide, such as garnet-type $Li_7La_3Zr_2O_{12}$,[10] perovskite-type $Li_{0.5}La_{0.5}TiO_3$,[11] and sodium superionic conductor (NASCION)-type $Li_{1.5}Al_{0.5}Ge_{1.5}(PO_4)_3$.[12] Although oxide-based SEs have better electrochemical stability, they have poor contact with the CAMs and often require a small amount of liquid electrolyte to improve interfacial wettability, which is unfavorable for practical applications.[13]

Recently, crystalline halide SEs have emerged as strong candidates because of their higher oxidation potential (usually around 4.0 V vs Li/Li^+), good ionic conductivity at room temperature (10^{-4} to10^{-3} S cm^{-1}), and superior cold-pressing deformability, which strike a balance between the advantages of sulfide and oxide SEs.[14] Typically, crystalline halide SEs have the general formula Li_aMX_6 (M = Y, Zr, In, Yb, etc.; X = F, Cl, Br, and I; $1 \leq a \leq 3$).[15] For instance, Asano and co-workers have first described trigonal Li_3YCl_6 in which anion sublattice exhibits hexagonal close packing (hcp), achieving a high ionic conductivity of

---

L. Shen, J.-L. Li, W.-J. Kong, P. Xu, X.-Y. Huang, W.-Z. Huang, F. Fu, Y.-C. Le, C.-Z. Zhao, Q. Zhang
Tsinghua Center for Green Chemical Engineering Electrification
Beijing Key Laboratory of Green Chemical Reaction Engineering and Technology
Department of Chemical Engineering
Tsinghua University
Beijing 100084, China
E-mail: zcz@mail.tsinghua.edu.cn; zhang-qiang@mails.tsinghua.edu.cn

J.-L. Li, Y.-C. Le
Tanwei College
Tsinghua University
Beijing 100084, China

C.-X. Bi, H. Yuan, J.-Q. Huang
Advanced Research Institute of Multidisciplinary Science
Beijing Institute of Technology
Beijing 100081, China

The ORCID identification number(s) for the author(s) of this article can be found under https://doi.org/10.1002/adfm.202408571

DOI: 10.1002/adfm.202408571

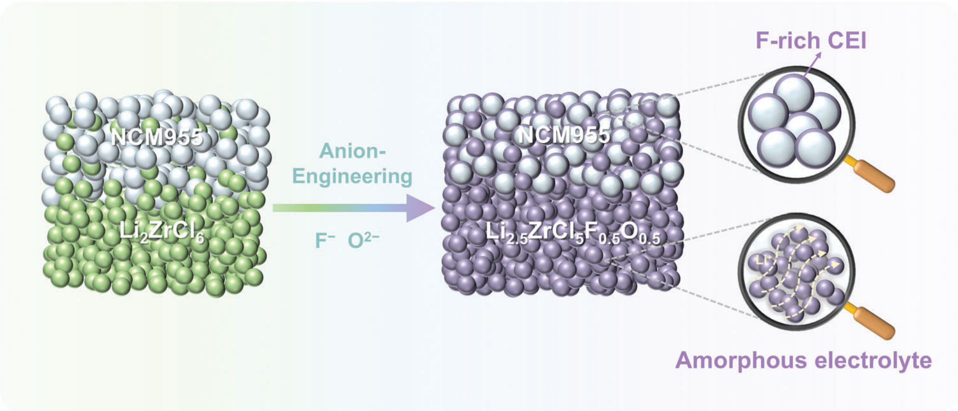

Figure 1. Scheme of high-voltage stable halide superionic conductor LZCFO for ASSLBs. The introduction of O^{2-} enhances amorphous species, provides a new Li^+ transport mechanism, and enhances ionic conductivity, and F^- promotes high-voltage stability and the formation of a robust F-rich CEI in ASSLBs.

0.51 mS cm^{-1} at 25 °C and constructing great interfacial compatibility with uncoated 4 V class $LiCoO_2$.[16] Further exploration has been conducted on non-lithium metal elements in recent years, promoting the exploration of halide SEs such as Li_3InCl_6 (1.49 mS cm^{-1} at 25 °C),[17] Li_3YbCl_6 (0.19 mS cm^{-1} at 30 °C),[18] and Li_2ZrCl_6 (0.40 mS cm^{-1} at 30 °C).[19]

Nevertheless, the oxidation potential of halide SEs cannot meet the requirements of high-voltage CAMs (e.g., 4.35 V for $LiNi_{0.9}Co_{0.05}Mn_{0.05}O_2$, NCM955),[20] and the poor interfacial compatibility results in serious cathode–electrolyte interfacial side reactions and reduces capacity and cycling stability of working ASSLBs.[21] Moreover, the ionic conductivity of halide SEs is unsatisfactory (often <1 mS cm^{-1}), resulting in a slow Li^+ transport and limiting the capacity and rate performance of ALLSBs.[22] It is challenging to achieve both the high-voltage stability and high ionic conductivity of crystalline halide SEs simultaneously. On the one hand, to enhance the high-voltage stability, it is necessary to employ elements such as F that are more electronegative than Cl.[23] Theoretical calculations have demonstrated that the oxidation potential of fluoride SEs is above 6 V versus Li/Li$^+$, which can effectively prevent the degradation of halide SEs at high voltage,[24] as well as generate F-rich components at the cathode–electrolyte interphase (CEI) to further inhibit the occurrence of side reactions.[25] However, the employment of F will strengthen the interactions between the anionic framework and Li^+ in the crystalline phase, which will drastically impair the ionic conductivity. On the other hand, isovalent or aliovalent cation substitution strategies (e.g., doping with Mg, Fe, Er, etc.) have been universally adopted to enhance the ionic conductivity of crystalline halide SEs.[26] Cation substitution allows modulation of the ratio of Li^+ to vacancy concentration and broadens the ionic transport paths in the lattice, therefore realizing the rapid Li^+ transport.[27] Unfortunately, the cation substitution strategies fail to change the mechanism of Li^+ transport in the crystalline phase and tend to have limited improvement in the high-voltage stability of halide SEs, because the source of degradation at high voltages is the anionic instability and oxidation. Consequently, new regulating approaches have to be evolved to address the dilemma of high-voltage stability and high ionic conductivity.

In this contribution, we exploited the anion-engineering of F^-/O^{2-} to implement the high-voltage stable halide superionic conductors and constructed high-performance ASSLBs with cost-effective Li_2ZrCl_6 (LZC) (**Figure 1**). F^- enhances the high-voltage stability of LZC thermodynamically and kinetically and fabricates the formation of a robust CEI. O^{2-} increases the amorphization of LZC, the highly disordered localized structure broadens the rapid Li^+ transfer mechanism, and breaks the restriction of Li^+ transport by the anionic framework in the routine crystalline phase mechanism, weakening the adverse effect of F^- on ionic conductivity. Consequently, the anion-engineering modified LZC ($Li_{2.5}ZrCl_5F_{0.5}O_{0.5}$, LZCFO) exhibits a practical electrochemical limit of 4.87 V versus Li/Li$^+$ while realizing an ionic conductivity of 1.17 mS cm^{-1} at 30 °C. The ASSLB assembled with NCM955 and LZCFO displays a high capacity of 207.1 mAh g^{-1} at 2.5–4.35 V versus Li/Li$^+$ and an excellent cycling stability of 81.2% capacity retention after 500 cycles at 0.5C. The interfacial evolution characterization indicates the formation of F-rich CEI, which suppresses the degradation of the SE and the side reactions at the cathode–electrolyte interfaces. This work provides a fresh insight into the design of SEs with high-voltage stability and high ionic conductivity and presents guidance for improving the cathode–electrolyte interface in working ASSLBs.

2. Results and Discussion

2.1. Synthesis and Characterizations of LZCFO

LZC was prepared via a ball-milling method of stoichiometric LiCl and $ZrCl_4$ as reported,[28] while $Li_{2.5}ZrCl_5F_{0.5}O_{0.5}$ (LZCFO) was synthesized with the extra addition of stoichiometric ZrF_4 and Li_2O to the raw material, where oxygen ions were selected to reduce crystallinity.[28,29] Meanwhile, the counterpart $Li_2ZrCl_{5.5}F_{0.5}$ (LZCF) or $Li_{2.5}ZrCl_{5.5}O_{0.5}$ (LZCO) were synthesized by adding stoichiometric ZrF_4 or Li_2O, respectively. As shown in Figure S1 (Supporting Information), X-ray Photoelectron Spectroscopy (XPS) measurements were conducted to confirm the chemical composition. The peaks of O 1s and F 1s are clearly present, indicating successful anion engineering. Meanwhile, the peaks of Li 1s, Cl 2p, and Zr 3d are basically unchanged, indicating that F^-/O^{2-} did not change the coordination mode of LZC. For the Zr 3d spectra, the peaks at 185.1 and 187.5 eV correspond to Zr^{4+} $3d_{3/2}$ and Zr^{4+} $3d_{5/2}$, respectively, confirming the tetravalent Zr in the electrolyte. In addition, the peaks related to O 1s at 531.5 and 530.1 eV can be assigned to Li–O and Zr–O.[30] These results demonstrated that O and F were fully involved in the coordination environments of the LZC. The scanning electron microscope (SEM) images demonstrate that all SEs are irregular nanoparticles with diameters ranging from 500 nm to 1 µm (Figure S1, Supporting Information). The corresponding energy dispersive spectrometer (EDS) elemental mappings illustrate the uniform distribution of Zr, Cl, F, and O, justifying sufficiently mechanochemical reactions (Figure S2 Supporting Information). X-ray diffraction (XRD) measurements of the four halide SEs were conducted to elucidate the crystalline status with Kapton film to prevent humidity (**Figure** 2a). Both LZC and LZCF exhibit a typical single-phase $P\bar{3}m1$ space group with an hcp anionic framework. The introduction of O^{2-} into the lattice leads to dual-phase features. The new diffraction signals appear for LZCO and LZCFO, which can be referred to as isostructures of the $C2/m$ space group, consistent with previous related reports.[29] The dual-phase LZCO and LZCFO have diffuser diffraction peaks, suggesting the generation of the amorphous phase (Figure S3, Supporting Information). To further analyze the crystalline status of the SEs, high-resolution XRD and corresponding Rietveld refinements of the four halide SEs were performed and the crystallinity was estimated (Figure S4, Supporting Information). As shown in Figure 2b, the crystallinity of LZC is 53.8%, while the crystallinity of LZCO is 30.0%, proving that the introduction of O^{2-} increases the amorphous content. The lowest crystallinity of 24.6% for LZCFO is attributed to the composition of multiple anions that promote localized disorder in the lattice structure, and such non-periodic localized structures are expected to enable fast Li^+ transport. The cryogenic transition electron microscope (cryo-TEM) images of LZC and LZCFO further convinced the considerable increase in amorphization. As shown in Figure 2c and Figure S5–S6 (Supporting Information), LZCFO features a smaller particle scale than LZC, and EDS elemental mappings exhibit that all elements are evenly dispersed in both LZC and LZCFO, in agreement with the SEM results. At a higher magnification, the presence of crystalline phases can be clearly observed in LZC, and selected area electron diffraction (SAED) exhibits the signals of polycrystal (Figure S7, Supporting Information). In contrast, as shown in Figure 2d,e, the lattice fringes of the crystalline phase are essentially unobserved in LZCFO, and there is only a weak signal of polycrystalline in SAED, indicating the abundant existence of amorphous phases in LZCFO.

The localized structural features of the highly amorphous halide electrolyte were further unraveled by X-ray absorption spectroscopy (XAS) measurements of LZC and LZCFO. As shown in Figure 2f, the main edge position of Zr K-edge X-ray absorption near-edge structure (XANES) spectra are all around 18020 eV, indicating the valence state for Zr^{4+}.[19] The whiteline feature of LZC displays three distinct splits, which are identical to those in $ZrCl_4$, indicating the presence of $[ZrCl_6]^{2-}$ coordinated octahedra in LZC just as in $ZrCl_4$. Nevertheless, the whiteline feature of LZCFO exhibits only a single peak, suggesting a disordered localized structural variation due to the anion-engineering of F^-/O^{2-}. As shown in Figure 2g, the Zr K-edge extended Fourier Transformed X-ray absorption fine structure (FT-EXAFS) spectra of LZC and LZCFO reveal peaks at around 2.0 Å for Zr–Cl coordination polyhedron (based on the Zr—Cl bond in $ZrCl_4$), while the spectrum of LZCFO exhibits an extra peak at around 1.5 Å, corresponding to the Zr—F/O bond (based on the Zr—F and Zr—O bond in ZrF_4 and ZrO_2, respectively). Furthermore, as shown in Figure 2h, the phase-uncorrected wavelet transformed (WT) EXAFS of LZCFO reconfirmed the coordination environments of Zr—F/O, Zr—Cl, and Zr—Zr at around 1.5, 2.0, and 3.2 Å, respectively, indicating the localized structure of $[ZrCl_aF_bO_c]^{(a+b+2c-4)-}$ coordination polyhedron in LZCFO. In contrast, the WT-EXAFS of LZC only displays signals for Zr—Cl and Zr—Zr, corresponding to $[ZrCl_6]^{2-}$ coordinated octahedra (Figure S8, Supporting Information). Consequently, both F and O are well-involved in the coordination of Zr, bringing about an abundance of localized disordered structures and amorphous components, and these non-periodic features can broaden the Li^+ transport mechanism and promote rapid Li^+ transport.

2.2. Electrochemical Properties of LZCFO

The extensive localized disordered structure afforded by amorphous species can potentially introduce a new mechanism for Li^+ conduction other than crystalline state mechanisms, weakening the constraints of the anionic framework on Li^+ transport and constructing SEs with high ionic conductivity. To validate the suspicion, the ionic conductivities of the four electrolytes at 30 °C were determined by the electrochemical impedance spectroscopy (EIS) measurements (**Figure** 3a). The ionic conductivity of LZC is 0.35 mS cm^{-1}, whereas that of LZCO is 1.39 mS cm^{-1}, which fully illustrates the facilitation of ionic conduction by high amorphization. The ionic conductivity of LZCF reduces by 65% to only 0.12 mS cm^{-1} compared to LZC, reflecting the introduction of F^- greatly intensifies the interaction between the anionic framework and Li^+ in the crystalline phase, therefore reducing the Li^+ transport. However, the ionic conductivity of LZCFO decreases by only 16% compared with that of LZCO, still maintaining a high ionic conductivity of 1.17 mS cm^{-1}, which implies that the Li^+ transport in the amorphous phase mainly depends on the localized disordered structure, and the detrimental effect of the strong Li–F interactions on ionic conductivity is diluted. To confirm whether it is the amorphous phase that promotes Li^+ transport, both LZCO and LZCFO were thermally treated at 100 °C for 2 h to enhance crystallinity and measured the ionic conductivity. There is a significant decrease in the ionic conductivity of the electrolytes after heat treatment (Figure S9, Supporting Information). The ionic conductivity of LZCO reduces by 51.8% to 0.67 mS cm^{-1} and LZCFO decreases by 70.9% to 0.34 mS cm^{-1}, which is caused by the reduction in the proportion of amorphous phases with fast Li^+ transport. It is noteworthy that the ionic conductivity of LZCFO decreases rapidly after heat treatment compared to LZCO, which is attributed to the increased crystalline content that exacerbates the hindrance of F^- to Li^+ transport in the crystalline phase. The temperature-dependent Nyquist profiles (Figure S10, Supporting Information) and Arrhenius plots of the four SEs (Figure 3b) further indicate the difference in the Li^+ transport mechanisms between the crystalline and amorphous phases. The activation energy (E_a) of Li^+ transport is around

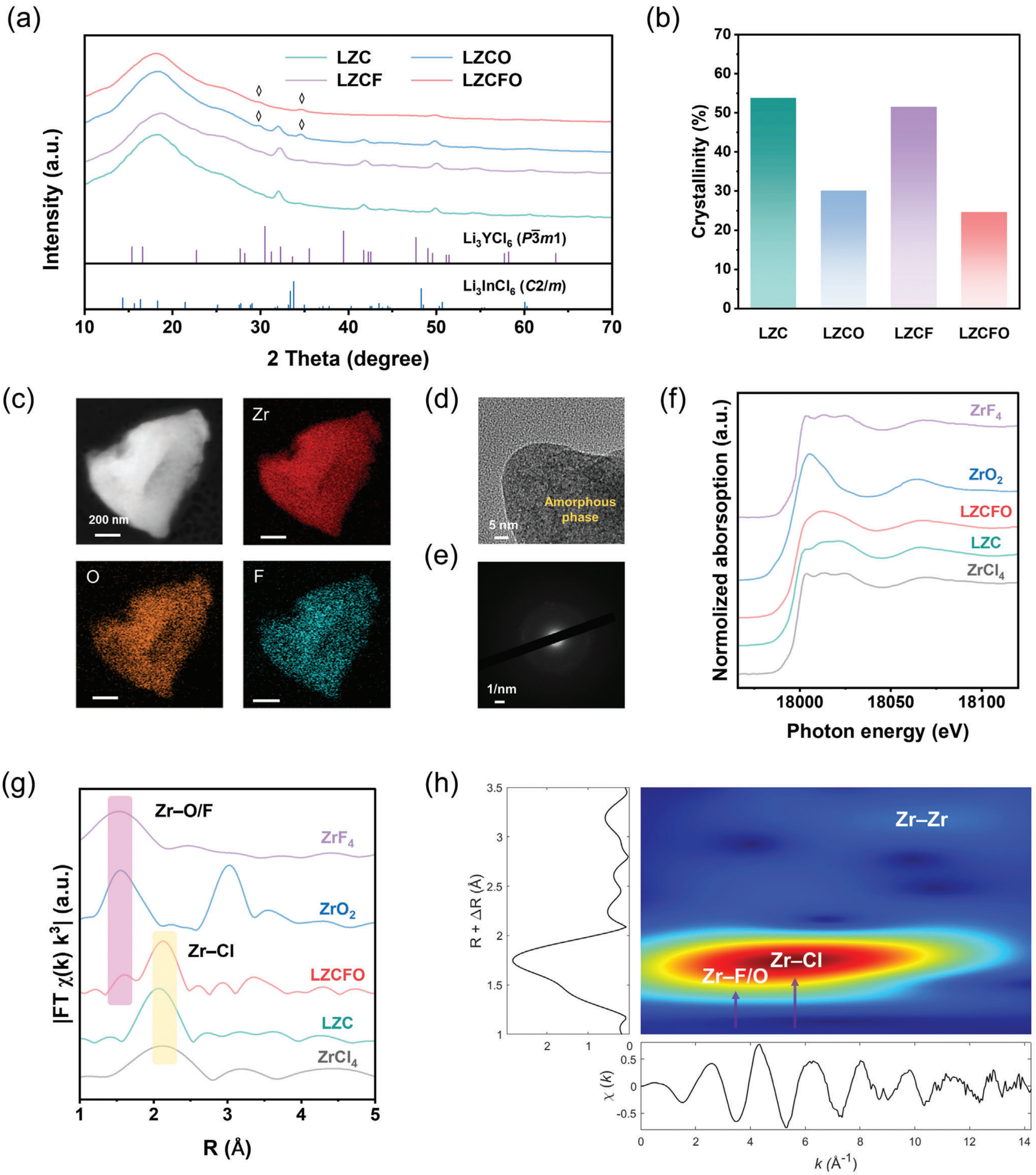

Figure 2. Material characterizations of LZCFO. a) XRD patterns and b) quantitative analysis of crystallinity of LZC, LZCO, LZCF, and LZCFO. c) Cyro-TEM images and corresponding EDS elemental mappings of LZCFO. d) High-resolution Cyro-TEM image of amorphous LZCFO and e) corresponding SAED pattern. f) Normalized Zr K-edge XANES spectra of LZC and LZCFO. g) FT of k^3-weighted Zr K-edge EXAFS spectra of LZC and LZCFO. h) WT-EXAFS spectrum of LZCFO at the Zr K-edge.

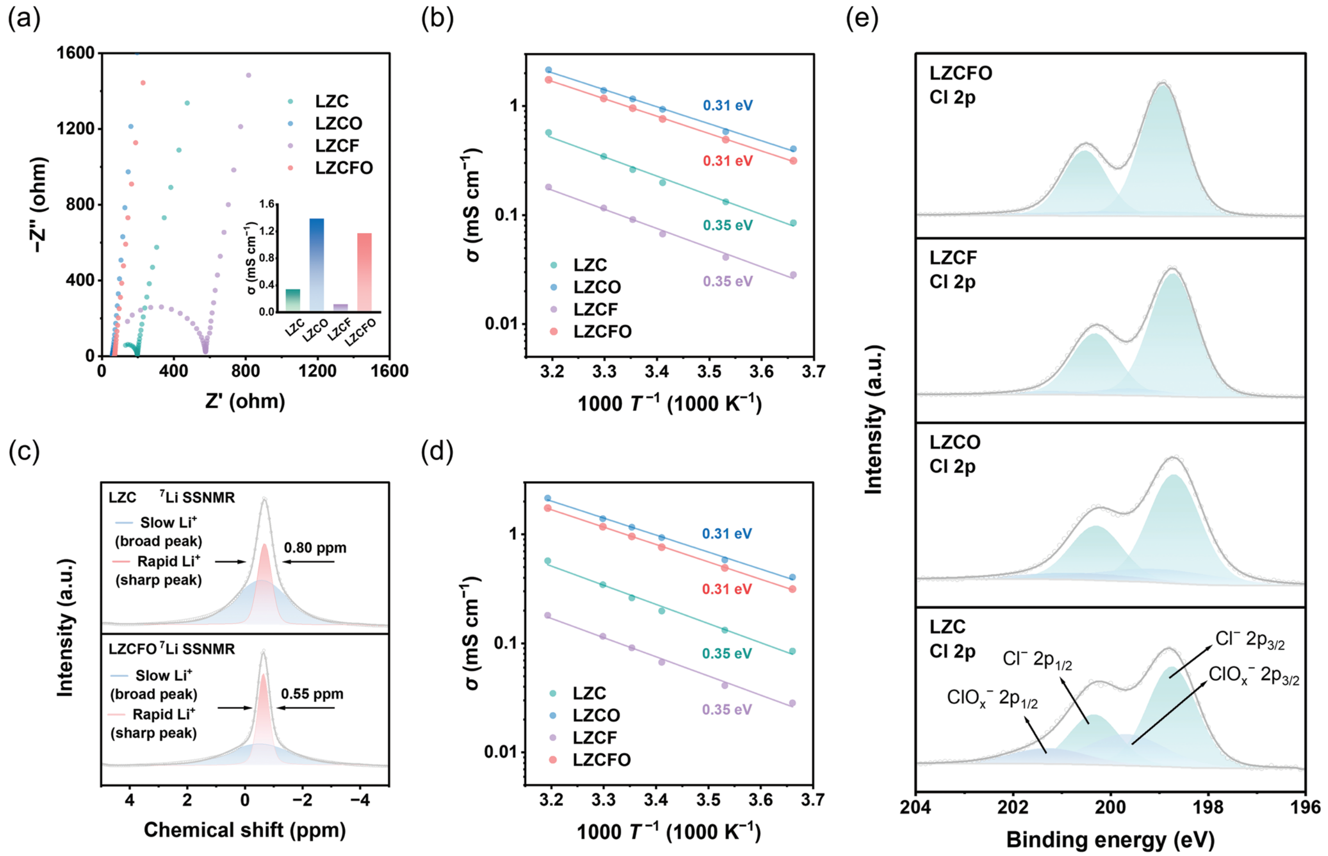

Figure 3. Electrochemical properties of LZCFO. a) The Nyquist plots of LZC, LZCO, LZCF, and LZCFO at 30 °C. The inset is the ionic conductivity of the four SEs. b) The Arrhenius plots of ionic conductivities for LZC, LZCO, LZCF, and LZCFO. c) The ^{7}Li SSNMR spectra of LZC and LZCFO: the sharp peak comes from fast-transport Li^+ and the broad one is due to slow-transport Li^+. d) LSV curves of LZC, LZCO, LZCF, and LZCFO. e) The deconvoluted Cl 2p XPS spectra of LZC, LZCO, LZCF, and LZCFO after LSV tests.

0.35 eV in crystalline phase dominated LZC and LZCF, while the E_a of the amorphous LZCO and LZCFO is around 0.31 eV, sufficiently illustrating the intrinsic advantage of Li^+ transport dependent on the short-range disordered structure. Meanwhile, ^{7}Li solid-state nuclear magnetic resonance (SSNMR) measurements of LZC and LZCFO were carried out in order to further justify the predominance of Li^+ transport in amorphous species (Figure 3c). Typically, the sharp Lorentzian peak represents conductors for fast Li^+ transport, while the broad Gaussian peak represents slow Li^+ conduction in anisotropic environments.[31] Therefore, a narrower FWHM indicates a faster Li^+ transport.[32] Quantitative analyses of sharp and broad peak content (Figure S11, Supporting Information) and FWHM indicate that LZCFO includes more fast ionic conductor components (44.3%, vs 31.8% of LZC) and a narrower FWHM (0.55 ppm, vs 0.80 ppm of LZC). This is consistent with higher amorphization of LZCFO, demonstrating that the amorphous phase brings about a new Li^+ conduction mechanism other than crystalline state mechanisms and is expected to construct more adequate ionic transport pathways in ASSLBs.

On the other hand, cyclic voltammetry (CV) tests in Li | Li_6PS_5Cl | halide SE | halide SE–muti-walled carbon nanotube (9:1 at a weight ratio) cells were also evaluated to confirm the enhancement in high-voltage stability by introducing F^- in the short-range disordered structure. To prevent side reactions between the halide SE and lithium metal, a thin layer of Li_6PS_5Cl was inserted between them. As shown in Figure S12 (Supporting Information), the oxidation potential of LZCFO is 4.22 V versus Li/Li^+, while LZCO is 4.03 V versus Li/Li^+, and the oxidation current of LZCFO is also much lower, proof that F^- thermodynamically enhances the immunity of Zr-based halide SE against electrochemical oxidation. More importantly, as shown in Figure 3d, the linear sweep voltammetry (LSV) test followed by the CV test reveals that LZCFO can exhibit a high practical electrochemical limit (the voltage limit considering interfacial kinetics during cycling) of 4.87 V versus Li/Li^+, while the practical electrochemical limit of LZCO is still only 4.16 V versus Li/Li^+. The comparison of CV and LSV tests of LZCF and LZC reflected the same trend, suggesting that the introduction of F^- also kinetically enhances the high-voltage stability of the SEs, possibly due to the F-rich interphase produced during the first cycle obstructing subsequent electrochemical oxidation. Notably, both thermodynamically and kinetically, the oxidation potentials of LZC and LZCO are less than 4.35 V versus Li/Li^+ used for NCM955, which represents that LZC and LZCO are unsuitable for ASSLB with Ni-rich NCM, and will undergo severe SE decomposition and increase the impedance of ASSLB during cycling. Similarly, XPS measurements of the four SEs after LSV tests were performed to

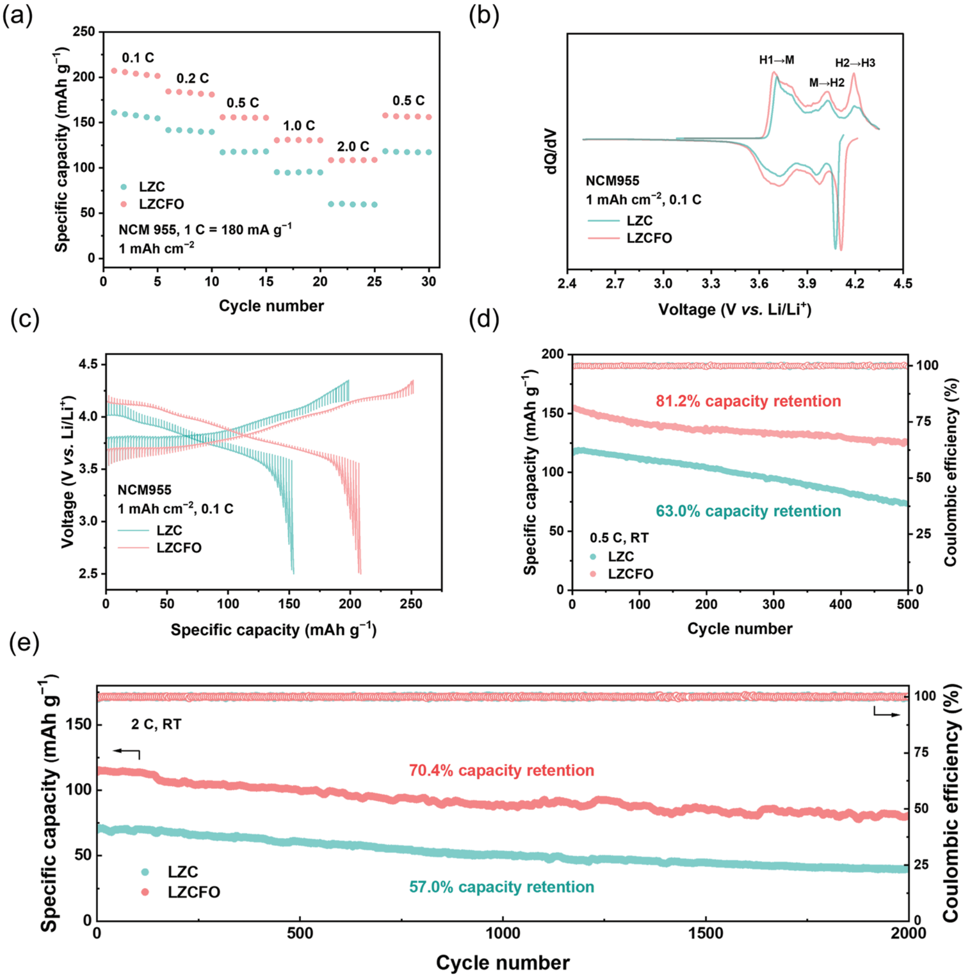

Figure 4. The electrochemical characterizations of ASSLBs. a) The rate performance, b) the GITT profiles for the 1st cycle at 0.1C, c) the d*Q*/d*V* profiles of the charge and discharge process for the 2nd cycle at 0.1C, d) the cycling performance at 0.5C, and e) cycling performance at 2.0C of the ASSLB with NCM955 and LZC or LZCFO.

analyze the decomposition conditions. The deconvoluted Cl 2p XPS spectra are shown in Figure 3e, in which the peaks at 198.9 and 200.5 eV correspond to Cl^- in the SE, whereas the peaks at 200.2 and 201.8 eV correspond to ClO_x^- that is oxidized and decomposed due to side reactions. The results of the quantitative analysis are shown in Figure S13 (Supporting Information). The proportions of ClO_x^- in LZCF and LZCFO are 8.3% and 6.5%, respectively, which were significantly lower than those in LZC and LZCO (32.8% and 22.5%, respectively), further corroborating that the introduction of F^- can prevent the SE from being oxidized.

2.3. Electrochemical Performance of ASSLBs

The high-voltage stable halide superionic conductor, LZCFO, should have excellent capacity and cycling stability in high-voltage ASSLBs. Therefore, Li-In | Li_6PS_5Cl | halide SE | halide SE–NCM955 (3:7 at a weight ratio) was assembled and evaluated between 2.5 and 4.35 V versus Li/Li^+ at room temperature. As shown in **Figure** 4a and Figures S14–S15 (Supporting Information), ASSLB with LZCFO exhibited the highest initial discharge capacity of 207.1 mAh g^{-1} at 0.1C (1C = 180 mA g^{-1}), while the ASSLB with LZC can only deliver a lowest discharge capacity of 161.0 mAh g^{-1}. Even at different rates of 0.2, 0.5, 1.0, and 2.0 C, the ASSLB with LZCFO maintained superior discharge capacities of 184.3, 155.8, 130.9, and 108.7 mAh g^{-1}, respectively. In contrast, the ASSLB with LZC can only exhibit capacities of 141.6, 118.0, 95.7, and 60.3 mAh g^{-1}, respectively. The ASSLB with LZCFO displayed optimal rate performance, which originates from the high ionic conductivity and high-voltage stability of LZCFO. The galvanostatic intermittent titration techniques (GITT) were employed to characterize the kinetic of ASSLB during the first charge and discharge processes (Figure 4b), and the polarization was quantitatively analyzed. In the galvanostatic charging process, ohmic polarization, activation polarization, and diffusion polarization will arise while being fully relaxed during the resting process, so it can be assumed that the termination voltage of the resting stage can reflect the thermodynamic voltage of the battery at this time, and the voltage drop in the relaxation process is the total polarization.[33] As shown in Figure S16 (Supporting Information), both during the charging and discharging processes, ASSLB with LZCFO always remained the minimum polarization, strongly demonstrating the electrode kinetic advances. Meanwhile, the effective diffusion coefficient of Li^+ ($D_{Li}+$) of the ASSLBs with LZC and LZCFO was calculated and shown in Figure S17 (Supporting Information). The $D_{Li}+$ during the charge and discharge process was in the range of 10^{-9} to 10^{-11} cm^2 s^{-1}, while $D_{Li}+$ of the ASSLBs with LZCFO was consistently higher than that of LZC at any voltage range, indicating the electrode kinetics advances of the ASSLB with LZCFO. The differential capacity (dQ/dV) profiles of the 2nd cycle at 0.1C of ASSLBs with the four SE are shown in Figure 4c to further investigate the kinetic behavior of ASSLB. Usually, the dQ/dV profiles respond to the structural evolution of the NCM955 during cycling, for instance, as the voltage rises there are respectively 1) from the original hexagonal phase to monoclinic phase (H1→M), 2) from monoclinic phase to the new hexagonal phase (M→H2), and 3) from hexagonal phase to another hexagonal phase (H2→H3) for the charging process.[34] The lower the voltage at which the phase transition occurs, the faster the electrode kinetic is. Compared to the ASSLB with LZC, the phase transition peaks of the ASSLB with LZCFO were shifted from 3.731, 4.033, and 4.214 V to 3.692, 4.025, and 4.192 V versus Li/Li^+, respectively, further indicating the kinetic superiority of the ASSLB with LZCFO, especially at the high voltage. To further deconvolute the effects of ionic conductivity and interfacial chemistry on the cathodic kinetics, we conducted EIS measurement in combination with distribution of relaxation time (DRT) analysis for ASSLB with LZC and LZCFO. The DRT technique is a powerful tool to analyze the resistance of individual processes, and the achieved relaxation-based function $\gamma(\tau)$ can distinguish specialized electrochemical processes by differences in relaxation times. Specifically, as shown in Figure S18 (Supporting Information), the peaks around 10^{-6} s correspond to the grain boundary response of LZC and LZCFO, the peaks at 10^{-5} to 10^{-4} s represent the contact resistance, the peaks around 10^{-3} to 10^{-2} s originating from the formation of solid electrolyte interphase (SEI), the peaks around 10^{-2} to 10^{-1} s originating from the formation of CEI, the peaks around 10^{-1} to 10^{0} s represents the charge transfer process, and the peaks around 10^{0} to 10^{1} s can be assigned to the diffusion resistance.[35] ASSLB with LZCFO has a smaller electrolyte grain boundary resistance, consistent with the ionic conductivity. Notably, ASSLB with LZCFO has smaller R_{CEI} and R_{Ct}, which indicates again that the stabilized interface at high voltage reduces interfacial impedance and facilitates charge transfer, leading to excellent cathodic kinetics.

Simultaneously, the high-voltage stability of LZCFO also contributes to the long cycling performance of the Ni-rich cathode. The long cycle profiles at 0.5C are shown in Figure 4d and Figure S19 (Supporting Information). The ASSLB with LZC exhibited an initial capacity of 116.5 mAh g^{-1} at 0.5C and only maintained 73.4 mAh g^{-1} after 500 cycles (63.0% capacity retention), while the ASSLB with LZCFO demonstrated an initial capacity of 154.9 mAh g^{-1} at 0.5C, and maintained 125.8 mAh g^{-1} after 500 cycles (81.2% capacity retention). The corresponding charge–discharge profiles showed that the ASSLB with LZCFO exhibited a slower capacity decay ratio and a higher discharge voltage (Figure S20, Supporting Information), indicating that the NCM955 with LZCFO kept structural stability during the repeated long cycling.

To verify the speculation of the high–voltage stability of SE affecting the structural stability of the NCM955, dQ/dV analysis was also performed on the ASSLBs at different cycle numbers at 0.5C.[36] As shown in Figure S21 (Supporting Information), the phase transition peaks of NCM955 are shifted with cycling, which represents a gradual collapse of the cathode structure and a consequent increase in polarization. Matched with high-voltage stable SE, the structural collapse of the NCM955 is significantly suppressed. For instance, the shifts of the two-phase transition peaks during the charging process decrease from 0.123 and 0.095 V of LZC to 0.077 and 0.076 V of LZCFO. The change of phase transition peaks during discharge conforms to the same pattern, indicating the protective effect of the high-voltage stable SE on the cathodes. Therefore, the ASSLB with LZCFO also displayed a high capacity retention of 70.4% after 2000 cycles even cycling at a high rate of 2.0C, compared to 57.0% of the ASSLB with LZC (Figure 4e; Figure S22, Supporting Information). The above electrochemical performance fully validates the application potential of high-voltage stable superionic conductors for optimizing capacity and cycling performance in ASSLBs.

2.4. Interfacial Evolution and Chemical Mechanisms

In order to gain a deeper understanding of the origin of the long cycling stability, high-resolution TEM images were recorded for the cycled NCM955 (discharged state) at 0.5C for 500 cycles with LZC and LZCFO. As shown in Figure S23 (Supporting Information), corresponding TEM images and EDS elemental mappings revealed a noticeable Ni, Co, and Mn distribution, reflecting that the particles were actually cycled NCM955. Further observation on the surface of the NCM955 with LZCFO exhibited a flat layer of CEI (**Figure** 5a; Figure S24, Supporting Information), covering the entire particle uniformly and protecting the cathodes from serious side reactions. However, the CEI of the cycled NCM with LZC was rugged and uneven with an inestimable thickness (Figure 5b; Figure S25, Supporting Information), indicating severe interfacial degradation. The ex situ XPS and time of flight secondary ion mass spectrometry (ToF-SIMS) measurements of cycled composite cathodes were further conducted to evaluate the chemical composition of the CEI. As shown in Figure 5c, the Ni^{2+} $2p_{3/2}$, Ni^{2+} $2p_{1/2}$, satellite $2p_{3/2}$, and satellite $2p_{1/2}$ peaks located at 853.6, 871.9, 862.7, and 880.9 eV, respectively, for the deconvoluted Ni 2p XPS spectrum of cycled NCM955 with LZCFO, which is consistent with literature reports.[37] The absence of Ni^{3+} originated from the full discharge of NCM955. In addition, two extra peaks were observed at 857.3 and 871.8 eV, which respectively corresponded to $2p_{2/3}$ and $2p_{1/2}$ of Ni—F bond,[38] indicating the generation of F-rich CEI. Such a highly stabilized CEI component effectively protected the NCM955 during cycling and prevented side reactions between the NCM955 and the SE. The deconvoluted Cl 2p XPS spectra also illustrated the suppression of side effects by F-rich CEI (Figure 5d). Only 10% of chlorine in SE is oxidized to ClO_x^- for cycled NCM955 with LZCFO, while 19% of chlorine in SE was oxidatively decomposed for cycled NCM955 with LZC. The proportion of ClO_x^- in SE for cycled NCM with LZCFO was consistently lower than that for cycled NCM with LZC even at different sputtering times (Figure S26, Supporting Information), further suggesting that the

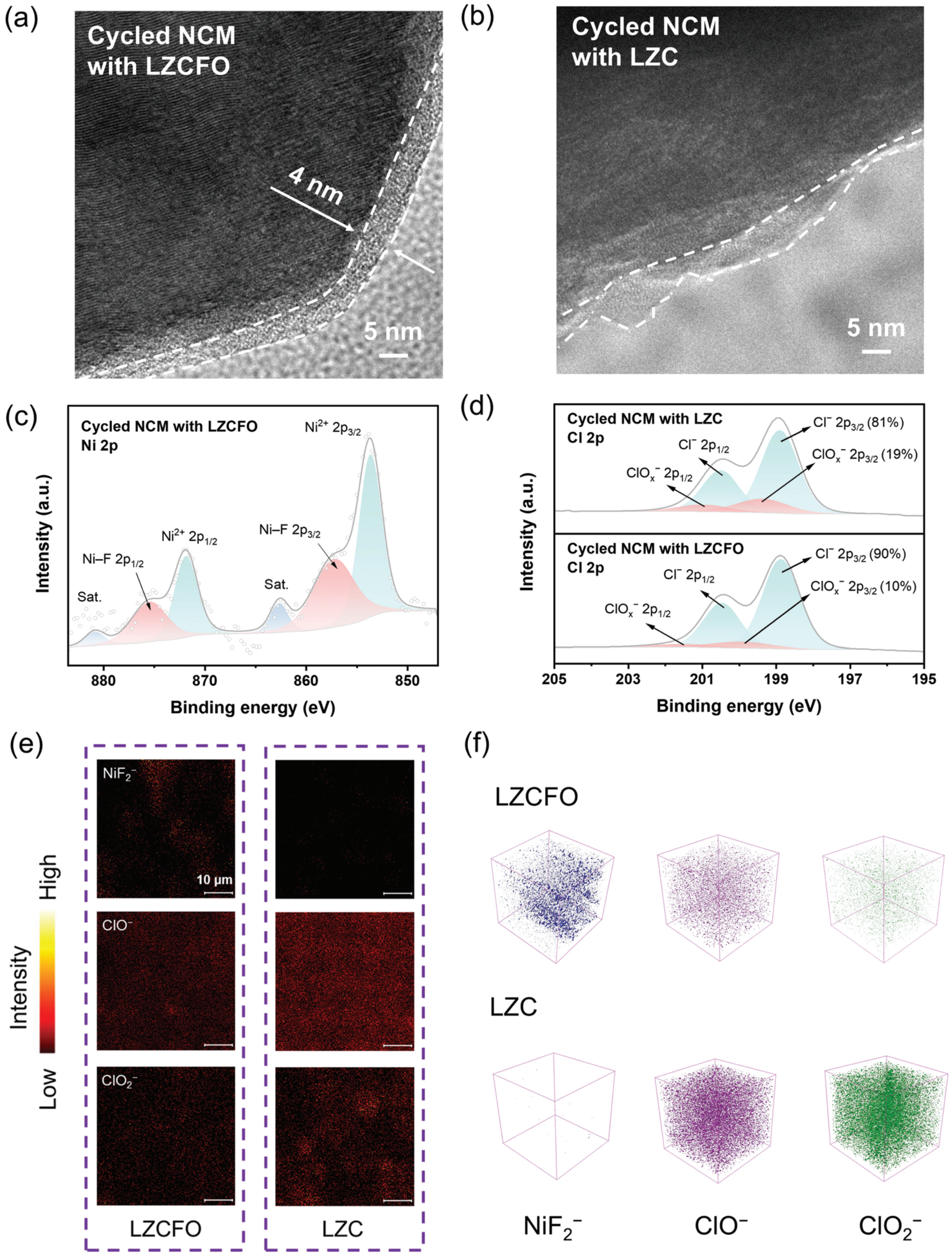

Figure 5. Interfacial chemical evolution between NCM955 and LZCFO. TEM images of cycled NCM955 with a) LZCFO and b) LZC. c) The deconvoluted Ni 2p XPS spectrum of cycled NCM955 with LZCFO. d) The deconvoluted Cl 2p XPS spectrum of cycled NCM955 with LZC and LZCFO. e) The ToF-SIMS analysis and f) 3D views of NiF_2^-, ClO^-, and ClO_2^- of cycled NCM955 with LZC and LZCFO.

uniform F-rich CEI avoids the oxidation of SE and protects the entire composite cathodes from degradation during high-voltage cycling. The ToF-SIMS measurements were further employed to complement the interfacial chemistry information, which has been demonstrated to be highly sensitive in characterizing the CEI composition and SE degradation.[39] As shown in Figure 5e, NiF_2^- fragments provided evidences for the formation of F-rich CEI, while ClO^- and ClO_2^- fragments quantified the SE degradation. The cycled NCM with LZCFO had a significant distribution of NiF_2^- and a much lower ClO^- and ClO_2^- content, consistent with the XPS spectra. The spatial distribution of each component was further resolved by 3D structure analysis (Figure 5f). The distribution of NiF_2^- in cycled NCM with LZCFO reflected the position of the NCM particles, while both ClO^- and ClO_2^- were uniformly distributed throughout the whole particle, illustrating the unfavorable effects of SE degradation on the composite cathodes. However, both ClO^- and ClO_2^- were similarly distributed throughout the whole space for cycled NCM with LZC, but at much higher concentration than cycled NCM with LZCFO, representing severe cathode–electrolyte side reactions and poor stability during high-voltage cycling. Consequently, the generation of F-rich CEI in the ASSLB with LZCFO was confirmed and effectively prevented the degradation at high voltages, enhancing the structural stability of the cathodes and the cycling stability of the ASSLB.

3. Conclusion

We have synthesized the high-voltage stable halide superionic conductor LZCFO based on an anion-engineering strategy for ASSLB. The F-rich interfaces promote high-voltage stability, and the highly amorphous species and disordered localized structures introduce the new Li^+ transport mechanism other than crystalline state mechanisms, which attenuates the detrimental effect of F^- on ionic conductivity. As a result, LZCFO achieved a practical electrochemical oxidation potential of 4.87 V versus Li/Li^+ and an ionic conductivity of 1.17 mS cm^{-1}. The ASSLB with NCM955 and LZCFO exhibited outstanding capacity, rate performance, and long cycling stability. The structural stability of NCM955 with LZCFO was further demonstrated and revealed that the F-rich CEI inhibited the side reactions between the cathode and the SE and reduced the decomposition of the SE, which ensures the stability of cycling at a high voltage. This work affords a fresh approach for the development of high ionic conductivity, high-voltage stable halide SEs and offers practical recipes for stable CEI in working ASSLB.

Supporting Information

Supporting Information is available from the Wiley Online Library or from the author.

Acknowledgements

L.S and J.-L.L. contributed equally to this work. This work was supported by the Beijing Municipal Natural Science Foundation (Z200011, L223009), National Key Research and Development Program (2021YFB2500300), National Natural Science Foundation of China (22393900, 22308190, 22309101, 22108151), Tsinghua-Jiangyin Innovation Special Fund (2022JYTH0101), China Postdoctoral Science Foundation (2023M731864, 2023M731920, 2022TQ0165), Tsinghua-Toyota Joint Research Fund, Young Elite Scientists Sponsorship Program by CAST (2021QNRC001), and the "Shuimu Tsinghua Scholar Program of Tsinghua University". The authors thank Zi-You Wang, Zi-Xuan Wang, Zi-Ning Cheng, Yu-Kun Liu, Jun-Dong Zhang, and Zong-Yao Shuang for their helpful discussions.

Conflict of Interest

The authors declare no conflict of interest.

Data Availability Statement

The data that support the findings of this study are available from the corresponding author upon reasonable request.

Keywords

all-solid-state lithium batteries, anion-engineering, cathode–electrolyte interphase, halide solid electrolyte, high-voltage stabililty

Received: May 18, 2024
Revised: July 18, 2024
Published online:

[1] a) D. Larcher, J. M. Tarascon, *Nat. Chem.* **2014**, *7*, 19; b) J. W. Choi, D. Aurbach, *Nat. Rev. Mater.* **2016**, *1*, 16013; c) F. Duffner, N. Kronemeyer, J. Tübke, J. Leker, M. Winter, R. Schmuch, *Nat. Energy* **2021**, *6*, 123; d) J. B. Goodenough, K.-S. Park, *J. Am. Chem. Soc.* **2013**, *135*, 1167.
[2] a) J. Janek, W. G. Zeier, *Nat. Energy* **2016**, *1*, 16141; b) S. Sun, C.-Z. Zhao, H. Yuan, Y. Lu, J.-K. Hu, J.-Q. Huang, Q. Zhang, *Mater. Futures* **2022**, *1*, 012101; c) L. Wu, Y. Wang, X. Guo, P. Ding, Z. Lin, H. Yu, *SusMat* **2022**, *2*, 264; d) W. J. Kong, C. Z. Zhao, S. Sun, L. Shen, X. Y. Huang, P. Xu, Y. Lu, W. Z. Huang, J. Q. Huang, Q. Zhang, *Adv. Mater.* **2023**, *36*, 2310738.
[3] a) X. Feng, H. Fang, N. Wu, P. Liu, P. Jena, J. Nanda, D. Mitlin, *Joule* **2022**, *6*, 543; b) Y.-S. Hu, *Nat. Energy* **2016**, *1*, 16042; c) S. Deng, M. Jiang, A. Rao, X. Lin, K. Doyle-Davis, J. Liang, C. Yu, R. Li, S. Zhao, L. Zhang, H. Huang, J. Wang, C. V. Singh, X. Sun, *Adv. Funct. Mater.* **2022**, *32*, 2200767.
[4] a) J. Chen, J. Wu, X. Wang, A. a. Zhou, Z. Yang, *Energy Storage Mater.* **2021**, *35*, 70; b) Q. Zhao, S. Stalin, C.-Z. Zhao, L. A. Archer, *Nat. Rev. Mater.* **2020**, *5*, 229.
[5] H. Yamane, M. Shibata, Y. Shimane, T. Junke, Y. Seino, S. Adams, K. Minami, A. Hayashi, M. Tatsumisago, *Solid State Ion.* **2007**, *178*, 1163.
[6] N. Kamaya, K. Homma, Y. Yamakawa, M. Hirayama, R. Kanno, M. Yonemura, T. Kamiyama, Y. Kato, S. Hama, K. Kawamoto, A. Mitsui, *Nat. Mater.* **2011**, *10*, 682.
[7] a) L. Zhou, N. Minafra, W. G. Zeier, L. F. Nazar, *Acc. Chem. Res.* **2021**, *54*, 2717; b) H. Yan, R. Song, R. Xu, S. Li, Q. Lin, X. Yan, Z. Wang, C. Yu, L. Zhang, *J. Energy Chem.* **2023**, *86*, 499; c) T. P. Poudel, M. J. Deck, P. Wang, Y. Y. Hu, *Adv. Funct. Mater.* **2023**, *34*, 2309656.
[8] J. Wu, S. Liu, F. Han, X. Yao, C. Wang, *Adv. Mater.* **2020**, *33*, 2000751.
[9] a) Y. Xiao, Y. Wang, S.-H. Bo, J. C. Kim, L. J. Miara, G. Ceder, *Nat. Rev. Mater.* **2019**, *5*, 105; b) A. Sakuda, A. Hayashi, M. Tatsumisago, *Chem. Mater.* **2009**, *22*, 949; c) Y. Nikodimos, C.-J. Huang, B. W. Taklu, W.-N. Su, B. J. Hwang, *Energy Environ. Sci.* **2022**, *15*, 991.
[10] a) V. Thangadurai, W. Weppner, *Adv. Funct. Mater.* **2005**, *15*, 107; b) R. Murugan, V. Thangadurai, W. Weppner, *Angew. Chem., Int. Ed.* **2007**, *46*, 7778.
[11] a) S. Stramare, V. Thangadurai, W. Weppner, *Chem. Mater.* **2003**, *15*, 3974; b) M. Itoh, Y. Inaguma, W. H. Jung, L. Q. Chen, T. Nakamura, *Solid State Ion* **1994**, *70*, 203.
[12] S. Xiong, Y. Liu, P. Jankowski, Q. Liu, F. Nitze, K. Xie, J. Song, A. Matic, *Adv. Funct. Mater.* **2020**, *30*, 2001444.
[13] a) Y. Nikodimos, W.-N. Su, B. W. Taklu, S. K. Merso, T. M. Hagos, C.-J. Huang, H. G. Redda, C.-H. Wang, S.-H. Wu, C.-C. Yang, B. J. Hwang, *J. Power Sources* **2022**, *535*, 231425; b) Z. Wan, D. Lei, W. Yang, C. Liu, K. Shi, X. Hao, L. Shen, W. Lv, B. Li, Q.-H. Yang, F. Kang, Y.-B. He, *Adv. Funct. Mater.* **2019**, *29*, 1805301; c) C. Wang, Q. Sun, Y. Liu, Y. Zhao, X. Li, X. Lin, M. N. Banis, M. Li, W. Li, K. R. Adair, D. Wang, J. Liang, R. Li, L. Zhang, R. Yang, S. Lu, X. Sun, *Nano Energy* **2018**, *48*, 35.
[14] a) C. Wang, J. Liang, J. T. Kim, X. Sun, *Sci. Adv.* **2022**, *8*, eadc9516; b) Y.-C. Yin, J.-T. Yang, J.-D. Luo, G.-X. Lu, Z. Huang, J.-P. Wang, P. Li, F. Li, Y.-C. Wu, T. Tian, Y.-F. Meng, H.-S. Mo, Y.-H. Song, J.-N. Yang, L.-Z. Feng, T. Ma, W. Wen, K. Gong, L.-J. Wang, H.-X. Ju, Y. Xiao, Z. Li, X. Tao, H.-B. Yao, *Nature* **2023**, *616*, 77; c) Y. Nikodimos, W. N. Su, B. J. Hwang, *Adv. Energy Mater.* **2022**, *13*, 2202854; d) K. Tuo, F. Yin, F. Mi, C. Sun, *J. Energy Chem.* **2023**, *87*, 12.
[15] J. Liang, X. Li, K. R. Adair, X. Sun, *Acc. Chem. Res.* **2021**, *54*, 1023.
[16] T. Asano, A. Sakai, S. Ouchi, M. Sakaida, A. Miyazaki, S. Hasegawa, *Adv. Mater.* **2018**, *30*, 1803075.
[17] X. Li, J. Liang, J. Luo, M. Norouzi Banis, C. Wang, W. Li, S. Deng, C. Yu, F. Zhao, Y. Hu, T.-K. Sham, L. Zhang, S. Zhao, S. Lu, H. Huang, R. Li, K. R. Adair, X. Sun, *Energy Environ. Sci.* **2019**, *12*, 2665.
[18] J. Park, D. Han, H. Kwak, Y. Han, Y. J. Choi, K.-W. Nam, Y. S. Jung, *Chem. Eng. J.* **2021**, *425*, 130630.

[19] H. Kwak, D. Han, J. Lyoo, J. Park, S. H. Jung, Y. Han, G. Kwon, H. Kim, S. T. Hong, K. W. Nam, Y. S. Jung, *Adv. Energy Mater.* **2021**, *11*, 2003190.
[20] Y. Gao, S. Zhang, F. Zhao, J. Wang, J. Zhou, W. Li, S. Deng, J. Fu, X. Hao, R. Li, X. Sun, *ACS Energy Lett.* **2024**, *9*, 1735.
[21] J. Liu, S. Wang, Y. Qie, Q. Sun, *Mater. Today Energy* **2021**, *21*, 100719.
[22] a) X. Luo, Y. Zhong, X. Wang, X. Xia, C. Gu, J. Tu, *ACS Appl. Mater. Interfaces* **2022**, *14*, 49839; b) K. Wang, Q. Ren, Z. Gu, C. Duan, J. Wang, F. Zhu, Y. Fu, J. Hao, J. Zhu, L. He, C.-W. Wang, Y. Lu, J. Ma, C. Ma, *Nat. Commun.* **2021**, *12*, 4410.
[23] a) T. Yu, Y. Duan, Y. Wu, Y. Liu, *J. Solid State Electrochem.* **2024**, *28*, 609; b) P. Ganesan, M. Soans, M. A. Cambaz, R. Zimmermanns, R. Gond, S. Fuchs, Y. Hu, S. Baumgart, M. Sotoudeh, D. Stepien, H. Stein, A. Groß, D. Bresser, A. Varzi, M. Fichtner, *ACS Appl. Mater. Interfaces* **2023**, *15*, 38391.
[24] a) S. Wang, Q. Bai, A. M. Nolan, Y. Liu, S. Gong, Q. Sun, Y. Mo, *Angew. Chem., Int. Ed.* **2019**, *58*, 8039; b) S. Kim, Y. Lee, K. Kim, B. C. Wood, S. S. Han, S. Yu, *ACS Energy Lett.* **2024**, *9*, 38.
[25] S. Zhang, F. Zhao, S. Wang, J. Liang, J. Wang, C. Wang, H. Zhang, K. Adair, W. Li, M. Li, H. Duan, Y. Zhao, R. Yu, R. Li, H. Huang, L. Zhang, S. Zhao, S. Lu, T. K. Sham, Y. Mo, X. Sun, *Adv. Energy Mater.* **2021**, *11*, 2100836.
[26] a) S. Chen, C. Yu, C. Wei, L. Peng, S. Cheng, J. Xie, *Chin. Chem. Lett.* **2023**, *34*, 107544; b) Q. Shao, C. Yan, M. Gao, W. Du, J. Chen, Y. Yang, J. Gan, Z. Wu, W. Sun, Y. Jiang, Y. Liu, M. Gao, H. Pan, *ACS Appl. Mater. Interfaces* **2022**, *14*, 8095; c) H. Zhang, Z. Yu, H. Chen, Y. Zhou, X. Huang, B. Tian, *J. Energy Chem.* **2023**, *79*, 348; d) S. Chen, C. Yu, S. Chen, L. Peng, C. Liao, C. Wei, Z. Wu, S. Cheng, J. Xie, *Chin. Chem. Lett.* **2022**, *33*, 4635.
[27] J.-D. Luo, Y. Zhang, X. Cheng, F. Li, H.-Y. Tan, M.-Y. Zhou, Z.-W. Wang, X.-D. Hao, Y.-C. Yin, B. Jiang, H.-B. Yao, *Angew. Chem., Int. Ed.* **2024**, *63*, 202400424.
[28] S. Zhang, F. Zhao, L.-Y. Chang, Y.-C. Chuang, Z. Zhang, Y. Zhu, X. Hao, J. Fu, J. Chen, J. Luo, M. Li, Y. Gao, Y. Huang, T.-K. Sham, M. D. Gu, Y. Zhang, G. King, X. Sun, *J. Am. Chem. Soc.* **2024**, *146*, 2977.
[29] L. Hu, J. Wang, K. Wang, Z. Gu, Z. Xi, H. Li, F. Chen, Y. Wang, Z. Li, C. Ma, *Nat. Commun.* **2023**, *14*, 3807.
[30] J. Cheng, H. Zhang, Z. Wang, Y. Zhou, K. Yu, Y. Cheng, Z. Yu, X. Huang, B. Tian, *J. Energy Storage* **2024**, *89*, 111700.
[31] a) P. Heitjans, M. Wilkening, *MRS Bull.* **2009**, *34*, 915; b) S. V. Patel, V. Lacivita, H. Liu, E. Truong, Y. Jin, E. Wang, L. Miara, R. Kim, H. Gwon, R. Zhang, I. Hung, Z. Gan, S.-K. Jung, Y.-Y. Hu, *Sci. Adv.* **2023**, *9*, eadj9930.
[32] F. Preishuber-Pflugl, M. Wilkening, *Dalton Trans.* **2016**, *45*, 8675.
[33] a) J. Shi, P. Li, K. Han, D. Sun, W. Zhao, Z. Liu, G. Liang, K. Davey, Z. Guo, X. Qu, *Energy Storage Mater.* **2022**, *51*, 306; b) J. Liang, Y. Zhu, X. Li, J. Luo, S. Deng, Y. Zhao, Y. Sun, D. Wu, Y. Hu, W. Li, T.-K. Sham, R. Li, M. Gu, X. Sun, *Nat. Commun.* **2023**, *14*, 146.
[34] Z.-X. Chen, Q. Cheng, X.-Y. Li, Z. Li, Y.-W. Song, F. Sun, M. Zhao, X.-Q. Zhang, B.-Q. Li, J.-Q. Huang, *J. Am. Chem. Soc.* **2023**, *145*, 16449.
[35] M. Yang, Y. Wu, K. Yang, Z. Wang, T. Ma, D. Wu, F. Xu, L. Yang, P. Lu, J. Peng, Q. Gao, X. Zhu, Z. Jiang, L. Chen, H. Li, F. Wu, *Adv. Energy Mater.* **2024**, *14*, 2303229.
[36] Y. Y. Wang, Z. Liang, Z. C. Liu, S. Liu, C. Ban, G. R. Li, X. P. Gao, *Adv. Funct. Mater.* **2023**, *33*, 2308152.
[37] a) J. Wang, Z. Zhang, J. Han, X. Wang, L. Chen, H. Li, F. Wu, *Nano Energy* **2022**, *100*, 107528; b) L. Wang, B. Huang, W. Xiong, M. e. Tong, H. Li, S. Xiao, Q. Chen, Y. Li, J. Yang, *J. Alloys Compd.* **2020**, *844*, 156034.
[38] B. P. Lochel, H. H. Strehblow, *J. Electrochem. Soc.* **1984**, *131*, 713.
[39] F. Walther, R. Koerver, T. Fuchs, S. Ohno, J. Sann, M. Rohnke, W. G. Zeier, J. Janek, *Chem. Mater.* **2019**, *31*, 3745.